Theoretical & Applied Mechanics Letters 7 (2017) 286–291

Contents lists available at ScienceDirect

Theoretical & Applied Mechanics Letters

journal homepage: www.elsevier.com/locate/taml

Letter

Stability of Couette flow past a gel film

Andrew Hess [a], Shengqiang Cai [b], Tong Gao [a,c,*]

[a] Department of Mechanical Engineering, Michigan State University, East Lansing, MI 48824, United States
[b] Department of Mechanical and Aerospace Engineering, University of California San Diego, La Jolla, CA 92093, United States
[c] Department of Computational Mathematics, Science and Engineering, Michigan State University, East Lansing, MI 48824, United States

ARTICLE INFO

Article history:
Received 1 September 2017
Accepted 14 September 2017
Available online 3 October 2017
*This article belongs to the Fluid Mechanics

Keywords:
Fluid-structure interaction
Hydrodynamic instability
Non-linear elasticity

ABSTRACT

We study instability of a Newtonian Couette flow past a gel-like film in the limit of vanishing Reynolds number. Three models are explored including one hyperelastic (neo-Hookean) solid, and two viscoelastic (Kelvin–Voigt and Zener) solids. Instead of using the conventional Lagrangian description in the solid phase for solving the displacement field, we construct equivalent "differential" models in an Eulerian reference frame, and solve for the velocity, pressure, and stress in both fluid and solid phases simultaneously. We find the interfacial instability is driven by the first-normal stress difference in the base-state solution in both hyperelastic and viscoelastic models. For the neo-Hookean solid, when subjected to a shear flow, the interface exhibits a short-wave (finite-wavelength) instability when the film is thin (thick). In the Kelvin–Voigt and Zener solids where viscous effects are incorporated, instability growth is enhanced at small wavenumber but suppressed at large wavenumber, leading to a dominant finite-wavelength instability. In addition, adding surface tension effectively stabilizes the interface to sustain fluid shear.

The interaction of viscous fluid and soft objects is of considerable importance in a wide range of problems, such as rheology of complex fluids, coating, biological locomotion, and soft lubrication [1–4]. When a soft material interacts with fluid flows, the coupling between the fluid force and material elasticity can generate waves propagating at the fluid/solid interface. Understanding this behavior is critical to the study of biological swimmers and their artificial analogs as it can greatly effect the viability and efficiency of a potential swimming mode. Kumaran et al. [5] first studied the stability of an incompressible viscoelastic gel film in a Newtonian Couette flow by ignoring inertia, where a linear model is adopted to describe deformation. They found the fluid/solid interface becomes unstable when the imposed shear goes beyond a certain critical number, and the critical value of the imposed fluid shear strength varies inversely with the film thickness for sufficiently thick solids, which is verified by the following experiments by Kumaran and Muralikrishnan [6,7]. For sufficiently thin solids, however, the linear elastic model overpredicts the critical values of the fluid shear that drives the interfacial instability. Gkanis and Kumar [8] studied the similar problem by employing a neo-Hookean solid model which admits finite/large deformation. While observing similar behaviors for thick gels, their model predicts a much smaller critical shear for thin gels, which suggests that incorporating solid nonlinearity can effectively destabilize the system. It has been identified that such interfacial instability under shear is mainly due to the first normal-stress difference appearing at the base state solutions, which is known as the Poynting effect in nonlinear solids [9,10], and is also similar to the situation of two coupled viscoelastic liquids [11,12]. When surface tension is incorporated into the model, it changes the short-wave instability in thin films to be finite-wavelength. Later Gkanis and Kumar [13] investigated how the flow field and combined pressure gradient impact stability of a neo-Hookean solid.

Although such elastohydrodynamic instability has been studied for simple neo-Hookean solids, in practice soft materials often exhibit more complicated constitutive behaviors than hyperelasticity. Especially for gel-like (e.g., hydrogel) materials that are typically composed of a large amount of solvent such as water and long chain polymers which can form a complex network by chemical crosslinkers such as covalent bond, or physical crosslinkers such as ionic bond or van der Waals interaction. The combined effects of elasticity, viscosity, and surface tension may generate new dynamic behaviors of the material [14], as well as some intriguing interfacial instability phenomena [15–17].

* Correspondence to: 428 S. Shaw Lane, Room 2555 East Lansing, Michigan 48824-1226, United States
E-mail address: gaotong@egr.msu.edu (T. Gao).

https://doi.org/10.1016/j.taml.2017.09.006

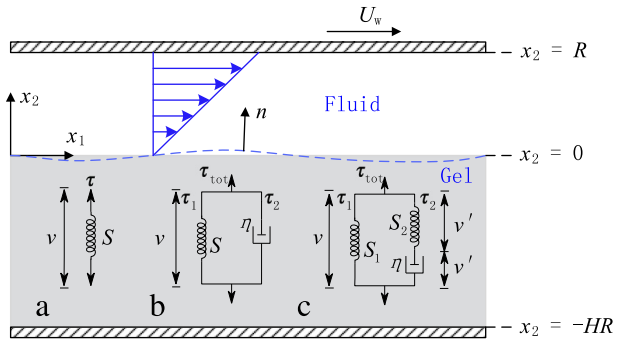

Fig. 1. Schematic for a Couette flow past a gel film. Nonlinear solid models: (a) neo-Hookean, (b) Kelvin–Voigt, (c) Zener.

In this paper we study stability of an incompressible, impermeable gel film when subjected to a Newtonian Couette flow; see schematic in Fig. 1. We employ an Eulerian representation in both fluid and solid phases, and solve for the velocity, pressure and stress fields simultaneously. Compared to the previous works [5,8,13], we examine the contributions from both the viscous effect and the nonlinear elasticity to the fluid/solid interface instability, especially for the thin films where material nonlinearity is manifested. The paper is organized as follows. We derive the evolution equations for the solid stress when using the neo-Hookean, Kelvin–Voigt, and Zener models. Next, we introduce the problem setup and non-dimensionalization, followed by details of a linear stability analysis. Then we discuss the results, and analyze the instability mechanism. Finally, conclusions and discussions are made.

We first derive equivalent "differential" models for the evolution equations of solid stress in an Eulerian frame. In this way, the governing equations in two phases are consistently defined in terms of velocity, pressure, and stress [4,18,19]. In characterizing material constitutive relations, virtual models of springs and dashpots are often employed to describe the contributions from the elastic and viscous effects, respectively. Different combinations of springs and dashpots can effectively represent complex viscoelastic behaviors as highlighted by the schematics for the three models (a–c) as shown in Fig. 1. The constitutive relation for the simplest nonlinear hyperelastic solid, i.e., neo-Hookean solid, can be characterized by a linear stress–strain relation $\boldsymbol{\tau}_{\rm nh} = S(\boldsymbol{B} - \boldsymbol{I})$ in a spring, where $\boldsymbol{\tau}_{\rm nh}$ is the elastic stress tensor, S is the shear modulus, and $\boldsymbol{B} = \boldsymbol{F}\cdot\boldsymbol{F}^{\rm T}$ is the Finger tensor where $\boldsymbol{F}$ (or index form $F_{ij} = \partial x_i/\partial X_j$) is the deformation gradient tensor serving as a mapping from the initial ($\boldsymbol{X}$) to the current ($\boldsymbol{x}$) reference frame. It is straightforward to show that the rate of change of the Finger tensor satisfies $\dot{\boldsymbol{B}} - \boldsymbol{L}\cdot\boldsymbol{B} - \boldsymbol{B}\cdot\boldsymbol{L}^{\rm T} = \boldsymbol{0}$, where $\boldsymbol{L} = \dot{\boldsymbol{F}}\cdot\boldsymbol{F}^{-1} = (\nabla\boldsymbol{v})^{\rm T}$ (here $L_{i,j} = \partial v_j/\partial x_i$) and dot represents the material time derivative $\dot{B}_{ij} = \partial B_{ij}/\partial t + v_k B_{ij,k}$. Then the differential form of the neo-Hookean model can be written as [19]:

neo-Hookean:

$$\boldsymbol{\tau}_{\rm nh}^{\nabla} = \dot{\boldsymbol{\tau}}_{\rm nh} - \boldsymbol{L}\cdot\boldsymbol{\tau}_{\rm nh} - \boldsymbol{\tau}_{\rm nh}\cdot\boldsymbol{L}^{\rm T} = S[\nabla\boldsymbol{v} + (\nabla\boldsymbol{v})^{\rm T}], \tag{1}$$

where $\boldsymbol{\tau}_{\rm nh}^{\nabla} = \dot{\boldsymbol{\tau}}_{\rm nh} - \boldsymbol{L}\cdot\boldsymbol{\tau}_{\rm nh} - \boldsymbol{\tau}_{\rm nh}\cdot\boldsymbol{L}^{\rm T}$ is the so called upper-convected time derivative.

To proceed, the simplest viscoelastic solid, a Kelvin–Voigt solid, can be characterized by connecting a spring with a dashpot in parallel. When deformed, each element exerts stress ($\boldsymbol{\tau}$) and undergoes deformation rate ($\boldsymbol{v}$) accordingly. The total stress of the element is hence defined by $\boldsymbol{\tau}_{\rm tot} = \boldsymbol{\tau}_1 + \boldsymbol{\tau}_2$, where $\boldsymbol{\tau}_1$ and $\boldsymbol{\tau}_2$ are the stresses in the respective branches. By defining $\boldsymbol{\tau}_1 = \boldsymbol{\tau}_{\rm nh}$ from Eq. (1) and the viscous stress as $\boldsymbol{\tau}_2 = \eta[\nabla\boldsymbol{v} + (\nabla\boldsymbol{v})^{\rm T}]$ (η is a solid viscosity), we derive a two-equation model for a Kelvin–Voigt material:

$$\begin{aligned}\text{Kelvin–Voigt}: \quad & \boldsymbol{\tau}_{\rm tot} = \boldsymbol{\tau}_1 + \eta[\nabla\boldsymbol{v} + (\nabla\boldsymbol{v})^{\rm T}],\\ & \boldsymbol{\tau}_1^{\nabla} = S[\nabla\boldsymbol{v} + (\nabla\boldsymbol{v})^{\rm T}].\end{aligned} \tag{2}$$

However, this model is known to produce reasonable values of creep but incorrectly predicts the behavior of stress relaxation [20], which can be improved by adding a second neo-Hookean spring element (with modulus S_2) in series with the dashpot to provide a Zener model. Note that on the right branch, we need to consider individual velocities associated with the spring $\boldsymbol{v}'$ and the dashpot $\boldsymbol{v}''$, which are related to the total velocity $\boldsymbol{v}$ through $\boldsymbol{v} = \boldsymbol{v}' + \boldsymbol{v}''$. Therefore, the neo-Hookean stress in the right branch (spring 2) now satisfies $\boldsymbol{\tau}_2^{\nabla} = S_2(\nabla\boldsymbol{v}' + \nabla\boldsymbol{v}'^{\rm T})$; the viscous stress becomes $\boldsymbol{\tau}_2 = \eta(\nabla\boldsymbol{v}'' + \nabla\boldsymbol{v}''^{\rm T})$. Again, by making use of the fact that $\boldsymbol{\tau}_{\rm tot} = \boldsymbol{\tau}_1 + \boldsymbol{\tau}_2$, after some algebra we derived the governing equations for the total stress ($\boldsymbol{\tau}_{\rm tot}$) and the neo-Hookean ($\boldsymbol{\tau}_1$) stress on the left branch (spring 1) in the Zener model:

$$\begin{aligned}\text{Zener}: \quad & \boldsymbol{\tau}_{\rm tot} + \lambda_1\boldsymbol{\tau}_{\rm tot}^{\nabla} = \boldsymbol{\tau}_1 + \lambda_2(\nabla\boldsymbol{v} + \nabla\boldsymbol{v}^{\rm T}),\\ & \boldsymbol{\tau}_1^{\nabla} = S_1\left(\nabla\boldsymbol{v} + \nabla\boldsymbol{v}^{\rm T}\right),\end{aligned} \tag{3}$$

where $\lambda_1 = \frac{\eta}{S_2}$ and $\lambda_2 = \frac{\eta}{S_2}(S_1 + S_2)$.

Consider an incompressible Newtonian fluid past a gel film as shown in Fig. 1 with material constitutive relations constructed above. The fluid layer with thickness R is bounded by the solid at the bottom and a rigid wall on the top moving with a constant velocity $U_{\rm w}$. The solid gel with thickness HR is fixed on a rigid plate. Following Kumaran et al. [5] and Gkanis and Kumar [8], we use R as the length scale, neo-Hookean modulus S_1 as the pressure/stress scale, $\mu_{\rm f}/S_1$ as the time scale, and $RS_1/\mu_{\rm f}$ as the velocity scale. The Reynolds number is then defined by $Re = \rho_{\rm f}S_1R^2/\mu_{\rm f}^2$. We ignore the inertia effect ($Re \ll 1$), and assume the fluid flow is governed by the Stokes equation. The dimensionless governing equations can be written as:

$$\nabla\cdot\boldsymbol{v}_{\rm f} = 0, \quad -\nabla p_{\rm f} + \nabla^2\boldsymbol{v}_{\rm f} = \boldsymbol{0}, \tag{4}$$

where $p_{\rm f}$ and $\boldsymbol{v}_{\rm f}$ are the pressure and the velocity field in the fluid, respectively. The solid is assumed to be incompressible. The conservation of mass and momentum equations are written in the Eulerian frame as:

$$\nabla\cdot\boldsymbol{v}_{\rm s} = 0, \quad -\nabla p_{\rm s} + \nabla\cdot\boldsymbol{\tau}_{\rm s} = \boldsymbol{0}, \tag{5}$$

where $\boldsymbol{v}_{\rm s}$ and $p_{\rm s}$ are the dimensionless solid velocity and pressure, respectively. And $\boldsymbol{\tau}_{\rm s}$ is a total stress tensor. The constitutive equations for the Zener model become

$$\boldsymbol{\tau}_{\rm s} + \hat{\lambda}_1\boldsymbol{\tau}_{\rm s}^{\nabla} = \boldsymbol{\tau}_{\rm nh} + \hat{\lambda}_2(\nabla\boldsymbol{v}_{\rm s} + \nabla\boldsymbol{v}_{\rm s}^{\rm T}), \quad \boldsymbol{\tau}_{\rm nh}^{\nabla} = \nabla\boldsymbol{v}_{\rm s} + \nabla\boldsymbol{v}_{\rm s}^{\rm T}, \tag{6}$$

where $\hat{\lambda}_1 = \frac{S_1}{S_2}\frac{\eta_{\rm s}}{\mu_{\rm f}}$ and $\hat{\lambda}_2 = \left(\frac{S_1+S_2}{S_2}\right)\frac{\eta_{\rm s}}{\mu_{\rm f}}$ respectively represent the relaxation and viscous effects, and $\boldsymbol{\tau}_{\rm nh}$ represents the dimensionless neo-Hookean stress. Note that $\hat{\lambda}_1$ and $\hat{\lambda}_2$ are related to each other by $\hat{\lambda}_2 = \hat{\lambda}_1 + \eta_{\rm s}/\mu_{\rm f}$, and hence $\hat{\lambda}_1 < \hat{\lambda}_2$. Furthermore, in the limit $\hat{\lambda}_1 \to \hat{\lambda}_2 = \lambda$, it is easy to show that the above equations reduce to $\lambda(\boldsymbol{\tau}_{\rm s} - \boldsymbol{\tau}_{\rm nh})^{\nabla} + (\boldsymbol{\tau}_{\rm s} - \boldsymbol{\tau}_{\rm nh}) = \boldsymbol{0}$, or in the Lagrangian frame, $\lambda\frac{\rm d}{{\rm d}t}\left[\boldsymbol{F}^{-1}\cdot(\boldsymbol{\tau}_{\rm s} - \boldsymbol{\tau}_{\rm nh})\cdot\boldsymbol{F}^{-{\rm T}}\right] + \left[\boldsymbol{F}^{-1}\cdot(\boldsymbol{\tau}_{\rm s} - \boldsymbol{\tau}_{\rm nh})\cdot\boldsymbol{F}^{-{\rm T}}\right] = \boldsymbol{0}$. When there is no pre-stress applied on the gel, it is trivial to show that $\boldsymbol{\tau}_{\rm s} = \boldsymbol{\tau}_{\rm nh}$, i.e., reduction from the full Zener model to the neo-Hookean model. Therefore, the neo-Hookean model ($\hat{\lambda}_1 = \hat{\lambda}_2 = 0$) and the Kelvin–Voigt model ($\hat{\lambda}_1 = 0,\ \hat{\lambda}_2 \neq 0$) appear to be the two asymptotic limits of the Zener model.

To supplement the governing equations with boundary conditions, we assume periodicity in x_1-direction, and apply no-slip conditions on the top (moving) and bottom (stationary) rigid walls. The dimensionless wall velocity is $\boldsymbol{v}_{\rm f} = G\hat{\boldsymbol{e}}_1$ at $x_2 = 1$, where

$G = \mu_f U_w/RS_1$ characterizes the strength of the applied shear flow field on the solid. At the fluid/solid interface, the velocity and traction are continuous:

$$\boldsymbol{v}_f = \boldsymbol{v}_s, \quad \boldsymbol{\sigma}_f \cdot \boldsymbol{n} + T\kappa \boldsymbol{n} = \boldsymbol{\sigma}_s \cdot \boldsymbol{n}, \tag{7}$$

where $\boldsymbol{n}$ is the normal vector to the interface, T is the dimensionless surface tension scaled by S_1R and κ is the curvature of the interface scaled by R^{-1}. The Eulerian models derived above are equivalent to the conventional Lagrangian models which typically solve for the displacement field, and simplify the mathematical treatment of the fluid–solid coupling at the interface to permit a more straightforward implementation of the velocity and traction continuity conditions [18].

To perform a linear stability analysis, we need to derive the base-state solutions when the interface is flat. The steady-state velocity solution in the fluid is simply a planar Couette flow $\boldsymbol{v}_f = (v_1, v_2) = (Gx_2, 0)$, and the fluid stress is given by $\boldsymbol{\sigma}_f = -p_f\boldsymbol{I} + \boldsymbol{\tau}_f = \begin{pmatrix} -p_f & G \\ G & -p_f \end{pmatrix}$. In the solid, the base-state solutions can be derived by solving the initial transient dynamics during which a fully developed shear flow start exerting on the gel. For the neo-Hookean model ($\boldsymbol{\tau}_s = \boldsymbol{\tau}_{nh}$), the (symmetric) total stress tensor in the solid is defined as $\boldsymbol{\sigma}_s = -p_s\boldsymbol{I} + \boldsymbol{\tau}_{nh} = \begin{pmatrix} -p_s + \tau_{11}^{nh} & \tau_{12}^{nh} \\ \tau_{12}^{nh} & -p_s + \tau_{22}^{nh} \end{pmatrix}$. It is also reasonable to assume that during the initial transient, the induced velocity field is unidirectional, i.e., $\partial/\partial x_1 = 0$ and $\boldsymbol{v}_s = (v_1(x_2), 0)$. Then the constitutive equations in Eq. (6) reduce to

$$\frac{\partial \tau_{11}^{nh}}{\partial t} = 2\tau_{12}^{nh}\frac{\partial v_1}{\partial x_2}, \quad \frac{\partial \tau_{12}^{nh}}{\partial t} = \frac{\partial v_1}{\partial x_2}, \quad \frac{\partial \tau_{22}^{nh}}{\partial t} = 0. \tag{8}$$

When there is no pre-stress in the solid, i.e., $\tau_{ij}^{nh} = 0$ at $t = 0$, it is apparent that $\tau_{22}^{nh} = 0$. Next, integrating both sides of the remaining two stress equations leads to

$$\begin{aligned} \tau_{12}^{nh} &= \int_0^T \frac{\partial v_1}{\partial x_2} dt = \frac{\partial u_1}{\partial x_2} = G, \\ \tau_{11}^{nh} &= 2\int_0^T \tau_{12}^{nh}\frac{\partial v_1}{\partial x_2} dt = \int_0^T \frac{\partial \left(\tau_{12}^{nh}\right)^2}{\partial t} dt = G^2, \end{aligned} \tag{9}$$

where $u_1 = \int_0^T v_1 dt$ is the displacement. Thus the total stress tensor at equilibrium reads

$$\boldsymbol{\tau}_{nh} = \begin{pmatrix} \tau_{11}^{nh} & \tau_{12}^{nh} \\ \tau_{12}^{nh} & \tau_{22}^{nh} \end{pmatrix} = \begin{pmatrix} G^2 & G \\ G & 0 \end{pmatrix}. \tag{10}$$

In the Kelvin–Voigt model and the Zener model, since $\boldsymbol{v}_s = \boldsymbol{0}$ at equilibrium, Eq. (10) also serves as the base-state solution for the three solid models. Therefore, the base-state total stress can be written as

$$\boldsymbol{\sigma}_s = -p_s\boldsymbol{I} + \boldsymbol{\tau}_s = \begin{pmatrix} -p_s + G^2 & G \\ G & -p_s \end{pmatrix}. \tag{11}$$

Note that a first normal stress difference appears, i.e., $\tau_{11}^s - \tau_{22}^s = G^2$. At the flat interface (i.e., $\boldsymbol{n} = (0, 1)$), Eq. (7) reduce to $\boldsymbol{\sigma}_f \cdot \boldsymbol{n} = \boldsymbol{\sigma}_s \cdot \boldsymbol{n}$ and $p_f = p_s$.

A standard linear stability analysis is employed to study the growth of disturbances [21]. All physical disturbance variables f' can be expanded with respect to normal modes $f'(x_1, x_2, t) = \tilde{f}(x_2)\exp(ikx_1 + \alpha t)$, where $\tilde{f}$ is the complex-valued amplitude functions, k is the wavenumber, and α is the complex-valued growth rate. The governing equations in Eqs. (4)–(6) are linearized, and then transformed into the Fourier space for the disturbances of $(\tilde{\boldsymbol{v}}_f, \tilde{p}_f)$ in fluid and $(\tilde{\boldsymbol{v}}_s, \tilde{p}_s, \tilde{\boldsymbol{\tau}}_s, \tilde{\boldsymbol{\tau}}_{nh})$ in solid. After some algebra, we are able to derive two fourth-order ordinary differential equations for the vertical velocity components $\tilde{v}_2^f$ and $\tilde{v}_2^s$ which admit the following general solutions:

$$\begin{aligned} \tilde{v}_2^f = {} & A_1\exp(kx_2) + A_2\exp(-kx_2) + A_3x_2\exp(kx_2) \\ & + A_4x_2\exp(-kx_2), \end{aligned} \tag{12}$$

$$\begin{aligned} \tilde{v}_2^s = {} & B_1\exp(kx_2) + B_2\exp(-kx_2) + B_3\exp(\xi_1x_2) \\ & + B_4\exp(\xi_2x_2), \end{aligned} \tag{13}$$

where $\xi_{1,2} = \frac{-iGk\left(1+\alpha\hat{\lambda}_1\right) \pm k\sqrt{-G^2\alpha\left(1+\alpha\hat{\lambda}_1\right)\left(\hat{\lambda}_1-\hat{\lambda}_2\right)+\left(1+\alpha\hat{\lambda}_2\right)^2}}{1+\alpha\hat{\lambda}_2}$, A_i and B_i ($i = 1, 2, 3, 4$) are eight unknown coefficients, four of which can be eliminated by boundary conditions at the two walls. For the neo-Hookean solid, we obtain $\xi_{1,2} = (-iG \pm 1)\,k$ independent of α, and again, recover the solutions obtained by Gkanis and Kumar [8].

The two solutions above are coupled through the kinematic condition

$$\frac{\partial \delta}{\partial t} + v_1\frac{\partial \delta}{\partial x_1} = v_2, \tag{14}$$

imposed at the perturbed interface $x_2 = \delta(x_1)$ where $|\delta| \ll 1$. It can be further linearized as $\frac{\partial \delta}{\partial t} = v_2'$ around the flat plane at $x_2 = 0$, and v_2' is the fluid (or solid) velocity disturbance. The velocity and traction continuity conditions lead to

$$v_1'^f + G\delta = v_1'^s, \tag{15}$$

$$v_2'^f = v_2'^s, \tag{16}$$

$$\frac{\partial v_1'^f}{\partial x_2} + \frac{\partial v_2'^f}{\partial x_1} + G^2\frac{\partial \delta}{\partial x_1} = \tau_{12}', \tag{17}$$

$$-p_f' + 2\frac{\partial v_2'^f}{\partial x_2} + T\frac{\partial^2 \delta}{\partial x_1^2} = -p_s' + \tau_{22}'. \tag{18}$$

The first normal stress difference from the base state (G^2) now appears at the left-hand-side of Eq. (17). The above equations are transformed using the normal modes to the Fourier space where we solve the growth rate α numerically for given values of H, k, T, G, $\hat{\lambda}_1$, and $\hat{\lambda}_2$.

Growth Rate. In Fig. 2, we show the real part of the growth rate of disturbance, Re(α), by varying thickness ratio (H), surface tension (T), and applied shear strength (G). When there is no surface tension at the interface ($T = 0$), for a thin solid ($H = 0.4$, panel (a)), Re(α) reaches a plateau at high wavenumber asymptotically, indicating a short wave instability. For a relatively thick film ($H = 4.0$, panel (b)), the maximum growth rate occurs at a finite k, hence indicating a finite-wavelength instability. Panels (c) and (d) show Re(α) as a function of k when surface tension is included, and chosen as $T = 10$. In both cases, the surface tension can effectively eliminate instability growth at high wavenumber. The obtained growth rates of the neo-Hookean model are identical to those obtained by Gkanis and Kumar [8].

Although the instabilities in panels (b)–(d) all appear to be finite-wavelength, their profiles are very different, leading to distinctive features shown later in the corresponding marginal-stability curves. In panel (b) where $T = 0$, while instability is induced at finite k and then more and more enhanced as the applied fluid shear G increases, the short-wave feature still remains as Re(α) saturates at large k. In panels (c) and (d) when $T \neq 0$, there are typically two separated regimes of peaks visible: One occurs at small k, and the other occurs at relatively large k. It is seen that with surface tension, the disturbance grows much faster at finite/large k regimes as G increases. Conversely, for thick films, instabilities appear to be more strengthened at small k.

Next, we consider the two viscoelastic models and make comparisons with the neo-Hookean model. The five cases presented in Fig. 3 follow a progression from the basic neo-Hookean model (black) to the Kelvin–Voigt model (red), and then to a full Zener model (blue). In the Kelvin–Voigt model where $\hat{\lambda}_1 = 0$ and $\hat{\lambda}_2 \neq 0$,

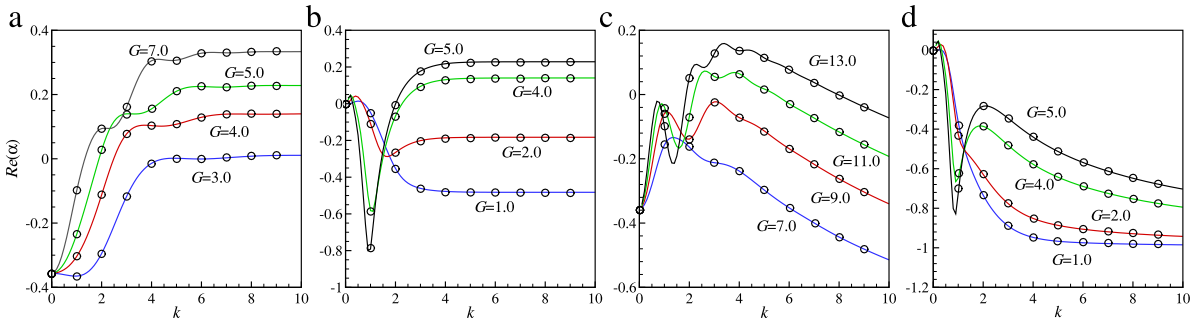

Fig. 2. The growth rate Re(α) as a function of k for the neo-Hookean solid: (a) $H = 0.4$, $T = 0$; (b) $H = 4.0$, $T = 0$; (c) $H = 0.4$, $T = 10$; (d) $H = 4.0$, $T = 10$. The open circles are the results obtained by Gkanis and Kumar [8].

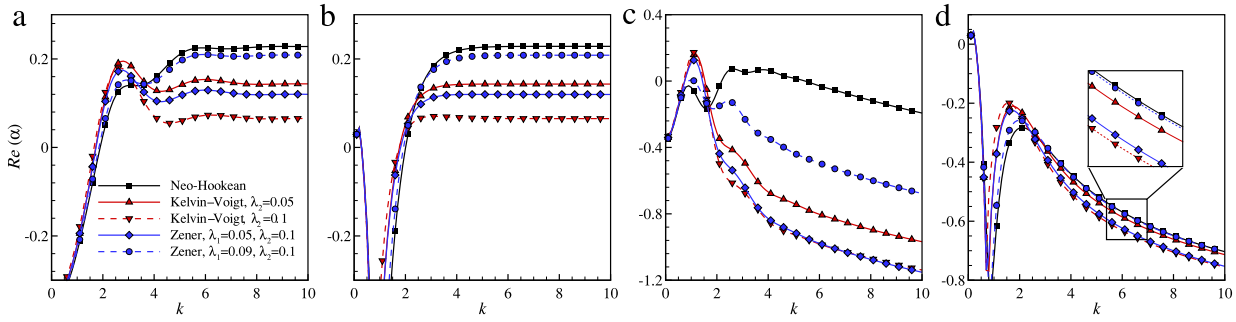

Fig. 3. Comparison of the growth rate Re(α) as a function of k for the neo-Hookean, Kelvin–Voigt, and Zener solids: (a) $H = 0.4$, $T = 0$, $G = 5$; (b) $H = 4.0$, $T = 0$, $G = 5$; (c) $H = 0.4$, $T = 10$, $G = 11$; (d) $H = 4.0$, $T = 10$, $G = 5$. (For interpretation of the references to colour in this figure legend, the reader is referred to the web version of this article.)

again, we find that increasing the effective solid viscosity (i.e., increasing $\hat{\lambda}_2$) suppresses instability at large k in both thin and thick gels, which makes the finite-wavelength instabilities dominate. On the other hand, in panels (a, c) we also observe that the instabilities are enhanced at finite wavenumbers to form local maximum for thin gels.

To examine the relaxation effect in the Zener model, we fix $\hat{\lambda}_2 = 0.1$ and vary the dimensionless relaxation time $\hat{\lambda}_1$. We observe that increasing $\hat{\lambda}_1$ shifts Re(α) upwards. As $\hat{\lambda}_1$ approaches $\hat{\lambda}_2$, this effect becomes increasingly pronounced and the curve gradually returns to that of the neo-Hookean model, consistent with the analytical predictions as $\hat{\lambda}_1 \to \hat{\lambda}_2$.

Mechanism. As noted by Gkanis and Kumar [8,13], the interfacial instability in the neo-Hookean solid is due to the coupling of the first normal stress difference and the surface fluctuation δ appearing in the interfacial condition. Here we adopt their explanation by considering a sinusoidal surface perturbation $\delta = \varepsilon \sin\left(\frac{2\pi}{k}x_1\right)$ as shown in the schematic in Fig. 4(a). The traction continuity condition in Eq. (17) essentially suggests the coupling term $G^2\delta_{x_1}$ has a 90° phase lag compared to velocity (and shape δ) fluctuations in Eq. (15), which tends to compress the wave crests and extend the valleys (marked by the black solid arrows), and hence destabilize the interface.

To understand the solid viscous effects in the Kelvin–Voigt model, we rewrite the shear stress component in Eq. (17) in the Fourier space as:

$$\tilde{\tau}_{12}^{\text{elast}} - \tilde{\tau}_{12}^{\text{f}} = G^2\tilde{\delta}_{x_1} - \tilde{\tau}_{12}^{\text{vis}} = \left[G^2 - \alpha\hat{\lambda}_2\left(\frac{D^2}{k^2}+1\right)\right]\tilde{\delta}_{x_1}. \tag{19}$$

In the above we split the solid stress $\boldsymbol{\tau}_s$ into the contributions from the hyperelastic (due to the neo-Hookean elasticity, and denoted by "elast") and viscous (due to the viscous term in the Kelvin–Voigt model, and denoted by "vis") effects. It is clearly seen that on the right-hand-side, as $k \to \infty$ the viscous term provides an asymptotic limit $-\alpha\hat{\lambda}_2$ acting against the first coupling term due to the normal stress difference. As illustrated by the red arrows in Fig. 4(a), this relaxes the pinching effect at large k to stabilize the surface though its behavior at small k is somewhat complex. A similar argument can be made based on the traction balance in the normal direction when examining the surface tension effect. Following the same procedure we rewrite Eq. (18) as

$$\tilde{\sigma}_{22}^{\text{elast}} - \tilde{\sigma}_{22}^{\text{f}} = T\tilde{\delta}_{x_1x_1} - \tilde{\sigma}_{22}^{\text{vis}} = \left(T + 2\alpha\hat{\lambda}_2\frac{D}{k^2}\right)\tilde{\delta}_{x_1x_1}. \tag{20}$$

The second derivative on δ results in a 180° phase shift so there is a normal force acting to restore the perturbed interface. Note that the right-hand-side of Eq. (20) can be written as $\left(-k^2T - 2\alpha\hat{\lambda}_2D\right)\tilde{\delta}$, suggesting that the contribution from the surface tension is scaled by k^2, and hence the inclusion of surface tension causes a significant damping effect to suppress disturbance growth, especially at large k [5,8].

Marginal Instability. We show the marginal stability curves for the critical shear stress G_c (Fig. 4(b)) and the corresponding critical wavenumber k_c (Fig. 4(c)) as functions of the film thickness ratio H. One obvious observation is that as H becomes large, all the models produce almost the same results as the linear elastic model [5] due to smaller deformation. We also observe that the marginal stability curves of the Zener model again vary between those of the neo-Hookean model and the Kelvin–Voigt model.

In panel (b) when surface tension is lacking, the three models in fact predict very similar values of G_c, suggesting that adding viscous effects to the solid does not necessarily stabilize the interface. In contrast, the finite-wavelength instabilities observed in Fig. 3(a) and (b) for the Kelvin–Voigt model may even cause a slight reduction in G_c, making the interface even more unstable under shear. The critical stresses for thin films are found to be around 2.93 while vary inversely with H for thick films, with transitions occurring for films with finite thickness ($H \approx 1$).

Adding surface tension effectively stabilizes the interface for all values of H, and yields finite-wavelength instabilities. Compared

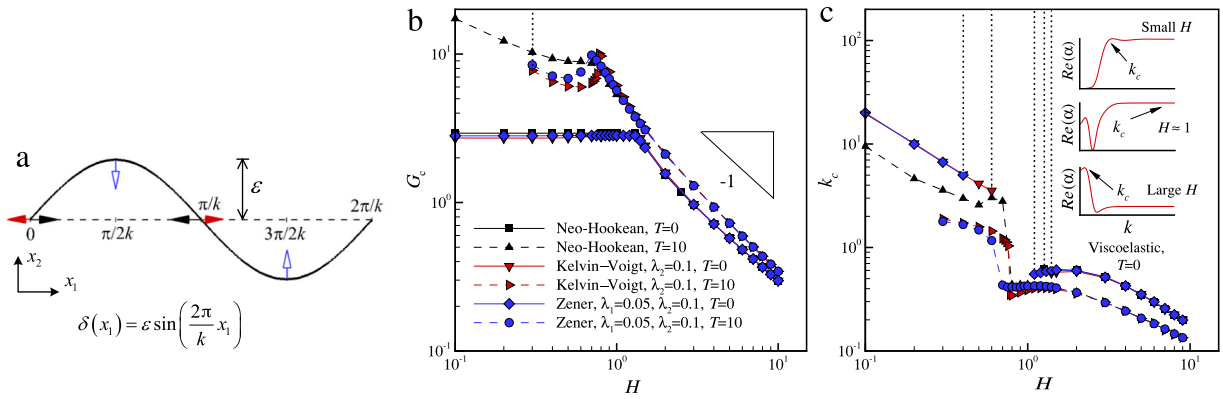

Fig. 4. (a) Schematic for a sinusoidal surface perturbation. The contributions of the first normal-stress difference and the solid viscous effect are marked by the black and red solid arrows, respectively. The open arrows represent the stabilizing effect due to surface tension. (b, c): Critical values of the imposed strain G_c and the critical wavenumber k_c as a function of H. The black dotted lines are drawn at the locations where either G_c or k_c tends to infinity. Inset in (c): Growth-rate curves near $H \approx 1$ where short-wave instabilities recur. (For interpretation of the references to colour in this figure legend, the reader is referred to the web version of this article.)

to the neo-Hookean model, the solid viscous effects significantly change the critical values for thin films, leading to yet more complex behaviors. When H is sufficiently small, we first identify a narrow regime where the system is stable to the fluid shear, i.e., $G_c \to \infty$ (marked by black dotted lines). At relatively large H, finite-wavelength instabilities appear, and predict lower critical values than the neo-Hookean case. As H further increases close to the transition regime, G_c rises again in both the Kelvin–Voigt and Zener models, up to maximum values around $H = 0.7$. Such non-monotonic behaviors are due to the amplification (suppression) of instability in the viscoelastic films at small (large) k as discussed in Fig. 3(c), which correspondingly picks relatively low (high) critical values of G_c for thin (thick) films.

While the $G_c - H$ curves are very similar, the marginal curves of k_c in panel (c) exhibit distinctive features between the three models at $T = 0$. At small thickness, the finite-wavelength instabilities in the two viscoelastic models are visible by the critical values of k_c beyond the stable regime; while $k_c \to \infty$ for the neo-Hookean solid due to its short-wave nature. Interestingly, we observe that in both the Kelvin–Voigt and Zener models, discontinuities of k_c occur near the transition regimes when $H \approx 0.7$, in accordance with the peaks in panel (b). As illustrated by the growth-rate curves in the inset of panel (c), in the transition regimes, increasing film thickness H drives a secondary finite-wavelength instability arising at small wavenumber. As the growth-rate maximum shifts from large towards small k, short-wave instabilities may recur, and hence k_c saturates at infinity, resembling those observed in the thin neo-Hookean films in Fig. 2. Moreover, inclusion of surface tension effectively reduces k_c as shown in the lower branch of marginal curves in panel (c). Also a stable regime at small H is identified for viscoelastic gels in accordance with panel (b) where G_c tends to infinity, and then finite-wavelength instabilities dominate as H increases.

In this paper, we investigate the interfacial stability of a soft gel film when subjected to a Newtonian Couette flow at zero Reynolds number. We have constructed three differential models for the solid stress including the neo-Hookean, Kelvin–Voigt, and Zener models, and solve for the velocity, pressure, and stress fields in both fluid and solid phases simultaneously in the Eulerian frame. We have performed linear stability analysis to study the interfacial instability by exploring the parameter spaces, and compared the critical behaviors of the three solid models. We focus our attention in the thin-film regime where the material nonlinearity is pronounced; while for sufficiently thick films, all the models produce very similar results as those predicted by linear models due to small deformation. We find the interfacial instability is driven by the first-normal stress difference in the base-state solution in the solid phase. Compared with the neo-Hookean model, inclusion of solid viscous effects leads to finite-wavelength instabilities in both thin and thick films, although we still observe short-wave instabilities recur in a narrow transition regime at finite film thickness. When surface tension is included, the fluid/solid interface becomes more stable, and finite-wavelength instabilities are found to dominate in all models. In addition, for viscoelastic gels we have observed stable regimes for sufficiently thin films, as well as intriguing non-monotonic features on the marginal stability curves near the transition regimes where the film thickness is finite.

It is interesting to observe that when surface tension is negligible, the critical values of the applied shear strength ($G_c \approx 2.93$) seem to be well-characterized by the neo-Hookean model, i.e., material's hyperelasticity. Further analysis reveals that the results obtained above can be directly extended to more general hyperelastic Mooney–Rivlin model which is used for constitutive relations in a wide range of materials. Recall the constitutive equation for a Mooney–Rivlin solid is given as $\boldsymbol{\tau}_s = g_1\boldsymbol{B} + g_2\boldsymbol{B}^{-1}$, where g_1 and g_2 are scalar functions of the invariants of $\boldsymbol{B}$ [22]. Thus the neo-Hookean model is a special case of the Mooney–Rivlin model by choosing $g_1 = 1$ and $g_2 = 0$. It is easy to show that $\boldsymbol{B}^{-1}$ satisfies a lower-convected derivative: $\dot{\boldsymbol{B}}^{-1} + \boldsymbol{L}^{\mathrm{T}}\boldsymbol{B}^{-1} + \boldsymbol{B}^{-1}\boldsymbol{L} = \boldsymbol{0}$ [23]. Following the same procedure as before, we find that a lower-convected model for the elastic stress $\boldsymbol{\tau}_s \propto \boldsymbol{I} - \boldsymbol{B}^{-1}$ yields the base-state solutions $\boldsymbol{\sigma}_s = \begin{pmatrix} -p_s & G \\ G & -p_s - G^2 \end{pmatrix}$ and $p_f = p_s + G^2$, which lead to identical stability analysis results as the neo-Hookean model where $\boldsymbol{\tau}_s \propto \boldsymbol{B} - \boldsymbol{I}$. Hence the Mooney–Rivlin model will generate the same results as the neo-Hookean model as well. With this study, it is straightforward to construct more elaborated solid models (e.g., poroelasticity), and apply similar methodologies to investigate their stabilities when coupled with fluid flows. It is also desired to perform direct simulations to resolve new physics and phenomena associated with nonlinear deformations in fluid/elastic-structure interactions.

Acknowledgments

T.G. acknowledges fruitful discussions with H.H. Hu, and the National Science Foundation (NSF) (DMS-1619960 and CBET-1702987). S.C. acknowledges NSF (CMMI-1538137).

References

[1] J. Zhang, S. Childress, A. Libchaber, et al., Flexible filaments in a flowing soap film as a model for one-dimensional flags in a two-dimensional wind, Nature 408 (2000) 835–838.

[2] B. Saintyves, T. Jules, T. Salez, et al., Self-sustained lift and low friction via soft lubrication, Proc. Natl. Acad. Sci. 113 (2016) 5847–5849.
[3] J.M. Skotheim, L. Mahadevan, Soft lubrication, Phys. Rev. Lett. 92 (2004) 245509.
[4] T. Gao, H.H. Hu, P.P. Castañeda, Shape dynamics and rheology of soft elastic particles in shear flow, Phys. Rev. Lett. 108 (2012) 058302.
[5] V. Kumaran, G.H. Fredrickson, P. Pincus, Flow-induced instability at the interface between a fluid and a gel at low reynolds number, J. Phys. II France 4 (1994) 893–911.
[6] V. Kumaran, R. Muralikrishnan, Spontaneous growth of fluctuations in the viscous flow of a fluid past a soft interface, Phys. Rev. Lett. 84 (2000) 3310–3313.
[7] R. Muralikrishnan, V. Kumaran, Experimental study of the instability of the viscous flow past a flexible surface, Phys. Fluids 14 (2002) 775–780.
[8] V. Gkanis, S. Kumar, Instability of creeping couette flow past a neo-hookean solid, Phys. Fluids 15 (2003) 2864–2471.
[9] L.A. Mihai, A. Goriely, Positive or negative poynting effect? the role of adscititious inequalities in hyperelastic materials, Proc. R. Soc. Lond. Ser. A Math. Phys. Eng. Sci. 467 (2011) 3633–3646.
[10] J.H. Poynting, On pressure perpendicular to the shear planes in finite pure shears, and on the lengthening of loaded wires when twisted, Proc. R. Soc. Lond. Ser. A Math. Phys. Eng. Sci. 82 (1909) 546–559.
[11] K. Chen, Elastic instability of the interface in couette flow of viscoelastic liquids, J. Non-Newton. Fluid Mech. 40 (1991) 261–267.
[12] Y. Renardy, Stability of the interface in two-layer couette flow of upper convected maxwell liquids, J. Non-Newton. Fluid Mech. 28 (1988) 99–115.
[13] V. Gkanis, S. Kumar, Stability of pressure-driven creeping flows in channels lined with a nonlinear elastic solid, J. Fluid Mech. 524 (2005) 357–375.
[14] C. Lai, Z. Zheng, E. Dressaire, et al., Elastic relaxation of fluid-driven cracks and the resulting backflow, Phys. Rev. Lett. 117 (2016) 268001.
[15] D. Chen, S. Cai, Z. Suo, et al., Surface energy as a barrier to creasing of elastomer films: An elastic analogy to classical nucleation, Phys. Rev. Lett. 109 (2012) 038001.
[16] S. Mora, T. Phou, J.M. Fromental, et al., Capillarity driven instability of a soft solid, Phys. Rev. Lett. 105 (2010) 214301.
[17] C. Xuan, J. Biggins, Finite-wavelength surface-tension-driven instabilities in soft solids, including instability in a cylindrical channel through an elastic solid, Phys. Rev. E 94 (2016) 023107.
[18] T. Gao, H.H. Hu, Deformation of elastic particles in viscous shear flow, J. Comput. Phys. 228 (2009) 2132–2151.
[19] T. Gao, H.H. Hu, P.P. Castañeda, Rheology of a suspension of elastic particles in a viscous shear flow, J. Fluid Mech. 687 (2011) 209–237.
[20] N.G. McCrum, C.P. Buckley, C.B. Bucknall, Principles of Polymer Engineering, Oxford University Press, 1997.
[21] S. Chandrasekhar, Hydrodynamic and Hydromagnetic Stability, Oxford University Press, 1961.
[22] C.W. Macosko, Rheology: Principles, Measurements and Applicatfons, VCH Publishers, New York, 1994.
[23] D.D. Joseph, Fluid Dynamics of Viscoelastic Liquids, in: Applied Mathematical Sciences, vol. 84, Springer Verlag, New York, 1990.